Available online at www.sciencedirect.com

ScienceDirect

IFAC PapersOnline CONFERENCE PAPER ARCHIVE

IFAC PapersOnLine 58-15 (2024) 55–60

Grey-box modelling and identification of the industrial oven of a shrink tunnel

Davide Previtali * **Leandro Pitturelli** * **Antonio Ferramosca** * **Fabio Previdi** *

* *Department of Management, Information and Production Engineering, University of Bergamo, Via G. Marconi 5, 24044 Dalmine (BG), Italy (e-mail: davide.previtali@unibg.it)*

Abstract: This paper presents a lumped-parameter grey-box sampled-data state-space model for the industrial oven of a shrink tunnel. The model is derived following the thermal-electrical analogy. A novel discretization strategy is developed to take into account that the sampling time of the system is equal to the lowest period of the pulse-width-modulated voltage signals which drive the heat resistors of the industrial oven. The model parameters are estimated by means of an extensive experimental campaign. Experimental results show that the derived model outperforms state-of-the-art transfer-function models while depending on fewer parameters.

Keywords: System identification and modelling, Grey-box modelling, Sampled-data models, Thermal network models, Discretization methods, Output-error identification, Shrink tunnel.

1. INTRODUCTION

Temperature control is widely diffused in disparate industrial sectors including metallurgy, manufacturing, chemical processes, food industry, and construction. Although most applications share the same goal, i.e. tracking a desired temperature profile, the controlled plants differ vastly, encompassing industrial furnaces (Tudon-Martinez et al. (2019)), convection ovens (Ramirez-Laboreo et al. (2016); Ryckaert et al. (1999)), Heating, Ventilation and Air Conditioning (HVAC) systems in buildings (Serale et al. (2018)), heat pumps (Rastegarpour et al. (2020)), heat exchangers (Vasičkaninová et al. (2011)), and environmental chambers (He et al. (2014)). Temperature control applications exhibit common characteristics. Firstly, the plants are divided into multiple control zones, each with its set of actuators and temperature sensors. Secondly, the control design is usually model-based (Serale et al. (2018)) such as Proportional-Integral-Derivative (PID) regulators or Model Predictive Control (MPC) strategies. Many different models are used, including:

- White-box models built from energy balance equations. For example, Rastegarpour et al. (2020) derived a nonlinear white-box model of a heat pump and employed it in an MPC strategy.
- Grey-box models, which still retain the physical description of the plant but require system identification methods to estimate the parameters. The most common are thermal network models (Sidebotham (2015)), which have been used, e.g., in Ramirez-Laboreo et al. (2016) to represent a convection oven.
- Black-box models, ranging from First Order Lag Plus time Delay (FOLPD) transfer functions to Artificial Neural Networks (ANNs). FOLPD models are broadly used due to their ease of PID tuning (Ryckaert et al. (1999); He et al. (2014)). Instead, ANNs are often employed in MPC strategies, e.g. in temperature control of heat exchangers (Vasičkaninová et al. (2011)) or in HVAC systems (Terzi et al. (2020)).

In this work, we focus on modelling the industrial oven of a shrink tunnel, a widely used application with a large impact on the packaging industry. Shrink tunnel control performances greatly affect plant energy consumption and are thus of utmost importance. Unfortunately, the tracking performances are often subpar due to the poor quality of the models used for control design. Shrink tunnels are composed of an industrial convection oven and a conveyor belt that feeds products (e.g. bottles) to it. The oven cavity is divided into different interconnected heating zones, each with multiple thermocouples and a dedicated set of heat resistors. Several convection fans allow for air circulation inside the cavity. Before being inserted into the oven, the products are wrapped in a thin plastic film. The heat within the cavity shrinks the plastic and tightly envelopes the products, creating the pack. Several relays drive the heat resistors by supplying Pulse-Width-Modulated (PWM) voltage signals. A common industry practice is to use a combination of ElectroMechanical Relays (EMRs) and Solid-State Relays (SSRs). The former are cheaper but exhibit lower switching rates (i.e. higher PWM periods) to prevent degradation. Consequently, the heat resistors driven by the EMRs typically track (on average) a desired temperature profile, while those controlled by the SSRs react to fast disturbances (e.g. the insertion of the products inside the oven cavity), preventing noticeable temperature drops.

In what follows, we derive a lumped-parameter grey-box sampled-data state-space model of a shrink tunnel, a relevant application that, to the best of our knowledge, has yet to be treated in the literature. In the present paper, we address the two main challenges of shrink tunnel modelling: (i) the presence of multiple PWM signals with different periods, and (ii) the restrictive experimental

10.1016/j.ifacol.2024.08.504

design conditions, mainly due to the long duration of the experiments that allow only open-loop step responses or closed-loop tracking experiments. The former challenge is solved via an ad hoc discretization method, the latter is tackled by performing multiple experiments, which are all taken into account when estimating the model parameters via the output-error approach (Verhaegen and Verdult (2007)).

This paper is organized as follows. Section 2 presents the shrink tunnel under study. Then, Section 3 describes the proposed model. The estimation of the model parameters is covered in Section 4. Next, Section 5 assesses the performances of the proposed model on experimental data, comparing it to a black-box FOLPD model. Lastly, Section 6 gives some concluding remarks.

2. SYSTEM DESCRIPTION

The shrink tunnel under study is used in bottle packs manufacturing processes. Its schematic is shown in Fig. 1, which highlights its main components. The oven cavity has a volume of $2.26\,\mathrm{m}^3$ and is divided into two interconnected heating zones. The heat in each zone is produced by a dedicated set of heat resistors, located in separate compartments. Specifically, each zone relies on one SSR and one EMR to modulate the voltages across the heat resistors. Two heating elements per zone are controlled by the same EMR. Instead, the SSRs drive four (respectively, two) heat resistors in zone 1 (zone 2). The relays are responsible for producing the voltage PWM signals based on the duty cycles supplied by a temperature controller. Due to the limitations of the electromechanical relays, the periods of the PWM signals are set to 30 s for the EMRs and 1 s for the SSRs respectively. The hot air in the proximity of the heat resistors diffuses inside the oven cavity by means of four convection fans installed at the top of the oven. The air temperature inside the oven is measured by six equally spaced thermocouples.

Let $i \in \{1,2\}$ be the zone of belonging. We denote the heat flow rate produced by the heat resistors in zone i at time $t \in \mathbb{R}_{\geq 0}$ (in s) as $q_i(t) \in \mathbb{R}_{\geq 0}$ (in $\frac{\mathrm{J}}{\mathrm{s}}$). Instead, $T_i^{(l)}(t) \in \mathbb{R}$ (in °C) is the temperature measured by the thermocouple positioned at location $l \in \{1,2,3\}$ in zone i at time t (see Fig. 1).

3. SHRINK TUNNEL MODEL

We consider the oven cavity divided into six subzones of the same volume, each with its own thermocouple (see Fig. 1). Based on this consideration, in Section 3.1 we propose a lumped-parameter state-space continuous-time model that describes the relationship between the heat produced by the heat resistors and the temperatures. Then, in Section 3.2, we derive its corresponding sampled-data model via a novel discretization method.

3.1 Continuous-time model

Following the thermal-electrical analogy (see Sidebotham (2015)), each subzone is modelled by an *RC*-analogue circuit; these are connected by a resistor that models the interaction between subzones. We assume that the heat produced by the heating elements originates from a specific location in each zone and then propagates throughout the whole oven cavity. Specifically, after several experiments, we have assessed that the hottest spots are located next to the thermocouples measuring $T_1^{(1)}$ and $T_2^{(2)}$ respectively. The resulting thermal network is shown in Fig. 1, where:

- $R_i^{(l)} \in \mathbb{R}_{>0}$ (in $\frac{^\circ\mathrm{C}}{\mathrm{J}} \cdot \mathrm{s}$), $i \in \{1,2\}, l \in \{1,2,3\}$, is the thermal resistance between the oven walls of zone i, location l, and the ambient;
- $R_{\mathrm{T}_i}^{(l')} \in \mathbb{R}_{>0}$ (in $\frac{^\circ\mathrm{C}}{\mathrm{J}} \cdot \mathrm{s}$), $i \in \{1,2\}, l' \in \{1,2\}$, is the thermal resistance related to the transfer of heat between two locations of zone i;
- $R_{\mathrm{T}_{21}} \in \mathbb{R}_{>0}$ (in $\frac{^\circ\mathrm{C}}{\mathrm{J}} \cdot \mathrm{s}$) is the thermal resistance related to the transfer of heat from zone 1 to zone 2;
- $R_{\mathrm{T}_{12}} \in \mathbb{R}_{>0}$ (in $\frac{^\circ\mathrm{C}}{\mathrm{J}} \cdot \mathrm{s}$) is analogous to $R_{\mathrm{T}_{21}}$ but going from zone 2 to zone 1; in general, $R_{\mathrm{T}_{21}} \neq R_{\mathrm{T}_{12}}$.
- $C_\mathrm{z} \in \mathbb{R}_{>0}$ (in $\frac{\mathrm{J}}{^\circ\mathrm{C}}$) is the thermal capacitance of the air in each subzone of the oven cavity, which all have the same volume.
- $T_\mathrm{a}(t) = \bar{T}_\mathrm{a}, \forall t \in \mathbb{R}_{\geq 0}, \bar{T}_\mathrm{a} \in \mathbb{R}$ (in °C), is the ambient temperature. It is constant during normal operation of the shrink tunnel;

The circuit in Fig. 1 includes two ideal diodes and two different thermal resistances $R_{\mathrm{T}_{21}}$ and $R_{\mathrm{T}_{12}}$ to model the possibility of having different static gains between the heat produced in one zone and the temperatures of the opposite zone. The system of differential equations governing the circuit in Fig. 1 is (Sidebotham (2015)):

$$\dot{\boldsymbol{T}}(t) = A_{TT} \cdot \boldsymbol{T}(t) + B_q \cdot \boldsymbol{q}(t) + \boldsymbol{b}_T \cdot T_\mathrm{a}(t), \qquad (1)$$

where $\boldsymbol{T}(t) \in \mathbb{R}^6$ amounts to

$$\boldsymbol{T}(t) = \left[T_1^{(3)}(t)\ T_1^{(2)}(t)\ T_1^{(1)}(t)\ T_2^{(1)}(t)\ T_2^{(2)}(t)\ T_2^{(3)}(t)\right]^\top,$$

$\dot{\boldsymbol{T}}(t) = \left[\frac{d}{dt}T_1^{(3)}(t)\ \ldots\ \frac{d}{dt}T_2^{(3)}(t)\right]^\top$, and $\boldsymbol{q}(t) = [q_1(t)\ q_2(t)]^\top$, $\boldsymbol{q}(t) \in \mathbb{R}^2_{\geq 0}$. Then, $A_{TT} \in \mathbb{R}^{6\times 6}$ is a matrix whose (i,j)-th entry $A_{TT}^{(i,j)}$ is zero except for:

$$A_{TT}^{(1,1)} = -\frac{1}{C_\mathrm{z}} \cdot \left[\frac{1}{R_1^{(3)}} + \frac{1}{R_{\mathrm{T}_1}^{(2)}}\right], \qquad A_{TT}^{(1,2)} = A_{TT}^{(2,1)} = \frac{1}{C_\mathrm{z}} \cdot \frac{1}{R_{\mathrm{T}_1}^{(2)}},$$

$$A_{TT}^{(2,2)} = -\frac{1}{C_\mathrm{z}} \cdot \left[\frac{1}{R_1^{(2)}} + \frac{1}{R_{\mathrm{T}_1}^{(2)}} + \frac{1}{R_{\mathrm{T}_1}^{(1)}}\right], \qquad A_{TT}^{(2,3)} = A_{TT}^{(3,2)} = \frac{1}{C_\mathrm{z}} \cdot \frac{1}{R_{\mathrm{T}_1}^{(1)}},$$

$$A_{TT}^{(3,3)} = -\frac{1}{C_\mathrm{z}} \cdot \left[\frac{1}{R_1^{(1)}} + \frac{1}{R_{\mathrm{T}_1}^{(1)}} + \frac{1}{R_{\mathrm{T}_{21}}}\right], \qquad A_{TT}^{(3,4)} = \frac{1}{C_\mathrm{z}} \cdot \frac{1}{R_{\mathrm{T}_{21}}},$$

$$A_{TT}^{(4,4)} = -\frac{1}{C_\mathrm{z}} \cdot \left[\frac{1}{R_2^{(1)}} + \frac{1}{R_{\mathrm{T}_2}^{(1)}} + \frac{1}{R_{\mathrm{T}_{12}}}\right], \qquad A_{TT}^{(4,3)} = \frac{1}{C_\mathrm{z}} \cdot \frac{1}{R_{\mathrm{T}_{12}}},$$

$$A_{TT}^{(5,5)} = -\frac{1}{C_\mathrm{z}} \cdot \left[\frac{1}{R_2^{(2)}} + \frac{1}{R_{\mathrm{T}_2}^{(2)}} + \frac{1}{R_{\mathrm{T}_2}^{(1)}}\right], \qquad A_{TT}^{(4,5)} = A_{TT}^{(5,4)} = \frac{1}{C_\mathrm{z}} \cdot \frac{1}{R_{\mathrm{T}_2}^{(1)}},$$

$$A_{TT}^{(6,6)} = -\frac{1}{C_\mathrm{z}} \cdot \left[\frac{1}{R_2^{(3)}} + \frac{1}{R_{\mathrm{T}_2}^{(2)}}\right], \qquad A_{TT}^{(5,6)} = A_{TT}^{(6,5)} = \frac{1}{C_\mathrm{z}} \cdot \frac{1}{R_{\mathrm{T}_2}^{(2)}}.$$

Lastly, $B_q \in \mathbb{R}^{6\times 2}$ is defined as:

$$B_q = \begin{bmatrix} 0 & 0 & \frac{1}{C_\mathrm{z}} & 0 & 0 & 0 \\ 0 & 0 & 0 & 0 & \frac{1}{C_\mathrm{z}} & 0 \end{bmatrix}^\top,$$

and $\boldsymbol{b}_T \in \mathbb{R}^6$ as:

$$\boldsymbol{b}_T = \frac{1}{C_\mathrm{z}} \cdot \left[\frac{1}{R_1^{(3)}}\ \frac{1}{R_1^{(2)}}\ \frac{1}{R_1^{(1)}}\ \frac{1}{R_2^{(1)}}\ \frac{1}{R_2^{(2)}}\ \frac{1}{R_2^{(3)}}\right]^\top.$$

The system of differential equations in (1) can be further extended by modelling the propagation of heat from the

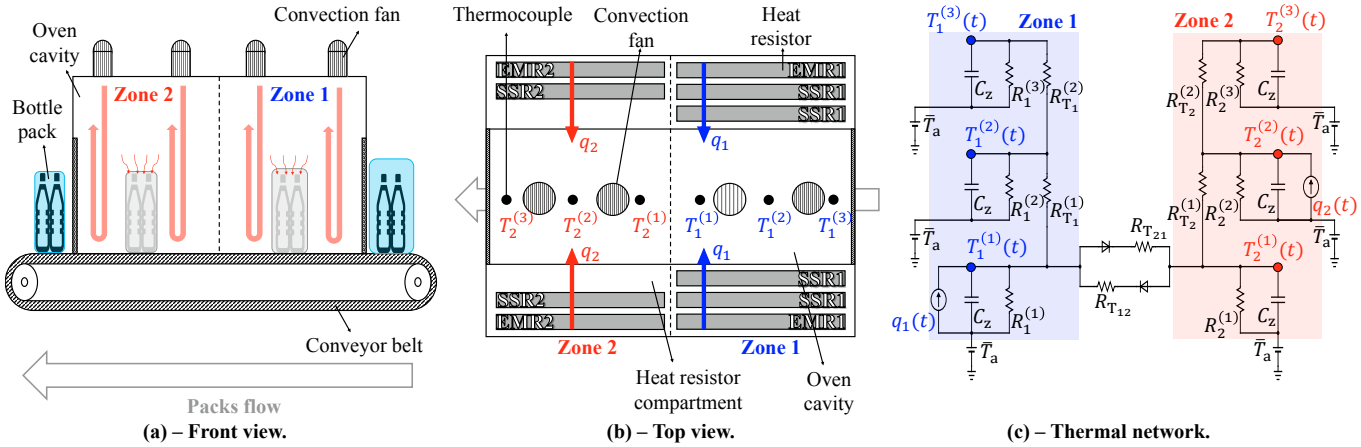

Fig. 1. Schematic of the considered shrink tunnel and associated thermal network. The heat resistors in zone $i, i \in \{1,2\}$, denoted by EMRi are driven by the same electromechanical relay while those denoted by SSRi are driven by the same solid-state relay.

heat resistors to the air inside the oven cavity using a first-order low-pass filter with unitary gain:

$$\dot{q}_i^{(\mathrm{f})}(t) = -\tau_i^{-1} \cdot q_i^{(\mathrm{f})}(t) + \tau_i^{-1} \cdot q_i(t), \quad \forall i \in \{1,2\}, \quad (2)$$

where $\tau_i \in \mathbb{R}_{>0}$ (in s) is the time constant for zone i. Then, in the circuit in Fig. 1, we should replace $q_i(t)$ with $q_i^{(\mathrm{f})}(t)$. The heat flow rates $\boldsymbol{q}(t)$ in (1) are generated by the heat resistors located in the corresponding zones. We consider the heat resistors in Fig. 1 in pairs: in the first zone, one pair is driven by the EMR and two pairs by the same SSR. Instead, in the second zone, the EMR and the SSR handle one pair each. We denote the voltages across the heat resistors as $V_i^{(r)}(t) \in \mathbb{R}_{\geq 0}$ (in V), where $i \in \{1,2\}$ denotes the zone while $r \in \{1,2\}$ indicates the driving relay ($r = 1$ for the SSRs and $r = 2$ for the EMRs). Let $R_{\mathrm{heat}} \in \mathbb{R}_{>0}$ (in Ω) be the resistance of a pair of heat resistors and assume that it is the same for each pair. Then:

$$q_1(t) = R_{\mathrm{heat}}^{-1} \cdot \left[2 \cdot V_1^{(1)}(t)^2 + V_1^{(2)}(t)^2\right], \quad (3a)$$

$$q_2(t) = R_{\mathrm{heat}}^{-1} \cdot \left[V_2^{(1)}(t)^2 + V_2^{(2)}(t)^2\right]. \quad (3b)$$

We group the $V_i^{(r)}(t)$'s in (3) inside a vector $\boldsymbol{V}(t)$,

$$\boldsymbol{V}(t) = \left[V_1^{(1)}(t)\ V_1^{(2)}(t)\ V_2^{(1)}(t)\ V_2^{(2)}(t)\right]^\top, \quad \boldsymbol{V}(t) \in \mathbb{R}^4_{\geq 0},$$

and define the vector of squared voltages as:

$$\boldsymbol{V}_{\mathrm{sq}}(t) = \boldsymbol{V}(t) \odot \boldsymbol{V}(t), \quad \boldsymbol{V}_{\mathrm{sq}}(t) \in \mathbb{R}^4_{\geq 0}, \quad (4)$$

where $\odot$ is the Hadamard product. By combining (1), (2), (3), and (4), we get the nonlinear state-space continuous-time model describing the shrink tunnel under study:

$$\begin{cases} \dot{\boldsymbol{q}}^{(\mathrm{f})}(t) = A_{ff} \cdot \boldsymbol{q}^{(\mathrm{f})}(t) + B_f \cdot \boldsymbol{V}_{\mathrm{sq}}(t) \\ \dot{\boldsymbol{T}}(t) = A_{TT} \cdot \boldsymbol{T}(t) + A_{Tf} \cdot \boldsymbol{q}^{(\mathrm{f})}(t) + \boldsymbol{b}_T \cdot T_{\mathrm{a}}(t) \\ \boldsymbol{y}(t) = \boldsymbol{T}(t) \end{cases}, \quad (5)$$

where $\boldsymbol{q}^{(\mathrm{f})}(t) = \left[q_1^{(1,\mathrm{f})}(t)\ q_1^{(2,\mathrm{f})}(t)\ q_2^{(1,\mathrm{f})}(t)\ q_2^{(2,\mathrm{f})}(t)\right]^\top \in \mathbb{R}^4_{\geq 0}$ is the vector of filtered heat flow rates associated with each $V_i^{(r)}(t)$, while $\boldsymbol{y}(t) \in \mathbb{R}^6$ are the outputs of the model (i.e. the temperatures). Lastly, the remaining matrices in (5) are defined as:

$$A_{ff} = \mathrm{diag}\left\{-\tau_1^{-1}, -\tau_1^{-1}, -\tau_2^{-1}, -\tau_2^{-1}\right\}, \quad A_{ff} \in \mathbb{R}^{4\times 4},$$

$$B_f = R_{\mathrm{heat}}^{-1} \cdot \mathrm{diag}\left\{\tau_1^{-1}, \tau_1^{-1}, \tau_2^{-1}, \tau_2^{-1}\right\}, \quad B_f \in \mathbb{R}^{4\times 4},$$

$$A_{Tf} = B_q \cdot \begin{bmatrix} 2 & 1 & 0 & 0 \\ 0 & 0 & 1 & 1 \end{bmatrix}, \quad A_{Tf} \in \mathbb{R}^{6\times 4}.$$

3.2 Sampled-data model

In what follows, we denote the PWM periods of the SSRs as $\mathcal{T}_{\mathrm{P}}^{(1)} = 1\,\mathrm{s}$ and those of the EMRs as $\mathcal{T}_{\mathrm{P}}^{(2)} = 30\,\mathrm{s}$. The signals of interest are sampled at a sampling time $\mathcal{T}_{\mathrm{s}} \in \mathbb{R}_{>0}$ such that $\mathcal{T}_{\mathrm{s}} = \mathcal{T}_{\mathrm{P}}^{(1)}$. Consequently, in this Section we will derive a sampled-data model for the system with sampling time $\mathcal{T}_{\mathrm{s}}$. We introduce the following notation:

- $s(t) \in \mathbb{R}$ is a continuous-time signal ($t \in \mathbb{R}_{\geq 0}$),
- $k \in \mathbb{N} \cup \{0\}$ is the discrete-time index,
- $\tilde{s}(k; \mathcal{T}_{\mathrm{s}}) \in \mathbb{R}$ is the discrete-time signal obtained by sampling $s(t)$ at a sampling time $\mathcal{T}_{\mathrm{s}}$. In particular, $\tilde{s}(k; \mathcal{T}_{\mathrm{s}}) = s(k \cdot \mathcal{T}_{\mathrm{s}}), \forall k \in \mathbb{N} \cup \{0\}$.

Before tackling the discretization of (5), consider the voltage PWM signals $V_i^{(r)}(t), i \in \{1,2\}, r \in \{1,2\}$. Each $V_i^{(r)}(t)$ has a duty cycle $u_i^{(r)}(t) \in [0,1]$ that (inherently) can be seen as a discrete-time signal sampled at a sampling time equal to its PWM period $\mathcal{T}_{\mathrm{P}}^{(r)}$. That is because:

$$u_i^{(r)}(t) = \tilde{u}_i^{(r)}\left(k; \mathcal{T}_{\mathrm{P}}^{(r)}\right), \quad \forall t : k \cdot \mathcal{T}_{\mathrm{P}}^{(r)} \leq t < [k+1] \cdot \mathcal{T}_{\mathrm{P}}^{(r)}.$$

Let $\tilde{\mathcal{T}}_{\mathrm{ON}_i}^{(r)}\left(k; \mathcal{T}_{\mathrm{P}}^{(r)}\right) \in \left[0, \mathcal{T}_{\mathrm{P}}^{(r)}\right]$,

$$\tilde{\mathcal{T}}_{\mathrm{ON}_i}^{(r)}\left(k; \mathcal{T}_{\mathrm{P}}^{(r)}\right) = \tilde{u}_i^{(r)}\left(k; \mathcal{T}_{\mathrm{P}}^{(r)}\right) \cdot \mathcal{T}_{\mathrm{P}}^{(r)}, \quad \forall k \in \mathbb{N} \cup \{0\}, \quad (6)$$

be the pulse active time at index k. Then, the corresponding voltage PWM signal is defined as:

$$V_i^{(r)}(t) = \begin{cases} V_{\mathrm{g}}(t) & \text{if } k \cdot \mathcal{T}_{\mathrm{P}}^{(r)} \leq t < k \cdot \mathcal{T}_{\mathrm{P}}^{(r)} + \tilde{\mathcal{T}}_{\mathrm{ON}_i}^{(r)}\left(k; \mathcal{T}_{\mathrm{P}}^{(r)}\right) \\ 0 & \text{if } k \cdot \mathcal{T}_{\mathrm{P}}^{(r)} + \tilde{\mathcal{T}}_{\mathrm{ON}_i}^{(r)}\left(k; \mathcal{T}_{\mathrm{P}}^{(r)}\right) \leq t < [k+1] \cdot \mathcal{T}_{\mathrm{P}}^{(r)} \end{cases} \quad (7)$$

where $V_{\mathrm{g}}(t) \in \mathbb{R}_{\geq 0}$ (in V) is the grid voltage. Fig. 2 shows an example of voltage PWM signals produced by the SSR and the EMR of zone 1. In order to discretize the system in (5), all signals must be sampled at the same sampling time $\mathcal{T}_{\mathrm{s}}$. However, the duty cycles of the EMRs

are inherently sampled at $\mathcal{T}_\mathrm{P}^{(2)} \neq \mathcal{T}_\mathrm{s}$. The next Section tackles the derivation of equivalent duty cycles for the EMRs that are suited for the discretization.

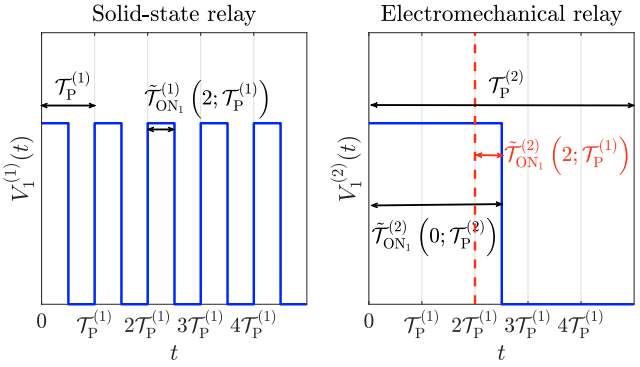

Fig. 2. Example of voltage PWM signals produced by the SSR and the EMR of zone 1. In this example, $\mathcal{T}_\mathrm{P}^{(1)} = 1\,\mathrm{s}$ and $\mathcal{T}_\mathrm{P}^{(2)} = 5\,\mathrm{s}$ (i.e. $\mathcal{T}_\mathrm{P}^{(2)} = 5 \cdot \mathcal{T}_\mathrm{P}^{(1)}$).

SSR-equivalent duty cycles for the EMRs. Let us assume that the PWM period of the EMRs is a multiple of the PWM period of the SSRs, i.e. $\mathcal{T}_\mathrm{P}^{(2)} = m \cdot \mathcal{T}_\mathrm{P}^{(1)}, m \in \mathbb{N}$. That is exactly the case for the system under study, for which $m = 30$. Then, we can see each PWM period of a EMR as a composition of m periods of a SSR. In particular, if we were to view the duty cycles $\tilde{u}_i^{(2)}\left(k;\mathcal{T}_P^{(2)}\right), i \in \{1,2\}$, sampled at $\mathcal{T}_\mathrm{s} = \mathcal{T}_\mathrm{P}^{(1)}$ rather than $\mathcal{T}_\mathrm{P}^{(2)}$, we would get:

$$\tilde{u}_i^{(2)}\left(k;\mathcal{T}_\mathrm{P}^{(1)}\right) = \begin{cases} 1 & \text{if } 0 \leq k \bmod m < \lfloor \kappa \rfloor \\ \gamma & \text{if } k \bmod m = \lfloor \kappa \rfloor \\ 0 & \text{if } \lceil \kappa \rceil \leq k \bmod m < m \end{cases}, \tag{8}$$

where:

$$\kappa = \tilde{\mathcal{T}}_{\mathrm{ON}_i}^{(2)}\left(k;\mathcal{T}_\mathrm{P}^{(2)}\right) \cdot \left(\mathcal{T}_\mathrm{P}^{(1)}\right)^{-1},$$
$$\gamma = \left[\tilde{\mathcal{T}}_{\mathrm{ON}_i}^{(2)}\left(k;\mathcal{T}_\mathrm{P}^{(2)}\right) \bmod \mathcal{T}_\mathrm{P}^{(1)}\right] \cdot \left(\mathcal{T}_\mathrm{P}^{(1)}\right)^{-1},$$

with mod being the modulo operation, while $\lfloor a \rfloor, \lceil a \rceil, a \in \mathbb{R}$, being the floor and ceiling functions respectively.

As an example, referring to Fig. 2 where $m = 5$ and $\tilde{\mathcal{T}}_{\mathrm{ON}_1}^{(2)}\left(0;\mathcal{T}_\mathrm{P}^{(2)}\right) = 2.5\,\mathrm{s}$, after applying (8) we get:

- $\tilde{u}_1^{(2)}\left(k;\mathcal{T}_\mathrm{P}^{(1)}\right) = 1$ for $k \in \{0,1\}$,
- $\tilde{u}_1^{(2)}\left(2;\mathcal{T}_\mathrm{P}^{(1)}\right) = 0.5$ (leading to $\tilde{\mathcal{T}}_{\mathrm{ON}_1}^{(2)}\left(2;\mathcal{T}_\mathrm{P}^{(1)}\right) = 0.5\,\mathrm{s}$),
- $\tilde{u}_1^{(2)}\left(k;\mathcal{T}_\mathrm{P}^{(1)}\right) = 0$ for $k \in \{3,4\}$.

Sampled-data model. Let us consider the duty cycles of the EMRs converted into their SSR equivalents using (8). We define the vector of duty cycles sampled at $\mathcal{T}_\mathrm{s} = \mathcal{T}_\mathrm{P}^{(1)}$, i.e. $\tilde{\boldsymbol{u}}(k;\mathcal{T}_\mathrm{s}) \in [0,1]^4$, as:

$$\tilde{\boldsymbol{u}}(k;\mathcal{T}_\mathrm{s}) = \left[\tilde{u}_1^{(1)}(k;\mathcal{T}_\mathrm{s})\ \tilde{u}_1^{(2)}(k;\mathcal{T}_\mathrm{s})\ \tilde{u}_2^{(1)}(k;\mathcal{T}_\mathrm{s})\ \tilde{u}_2^{(2)}(k;\mathcal{T}_\mathrm{s})\right]^\top.$$

In order to discretize the system under study, we integrate the left and the right sides of the differential equations in (5) between $k \cdot \mathcal{T}_\mathrm{s}$ and $(k+1) \cdot \mathcal{T}_\mathrm{s}$. For what concerns the filtered heat flow rates, we get:

$$\tilde{\boldsymbol{q}}^{(\mathrm{f})}(k+1;\mathcal{T}_\mathrm{s}) - \tilde{\boldsymbol{q}}^{(\mathrm{f})}(k;\mathcal{T}_\mathrm{s}) = A_{ff} \cdot \int_{k\cdot\mathcal{T}_\mathrm{s}}^{(k+1)\cdot\mathcal{T}_\mathrm{s}} \boldsymbol{q}^{(\mathrm{f})}(t)\,dt + B_f \cdot \int_{k\cdot\mathcal{T}_\mathrm{s}}^{(k+1)\cdot\mathcal{T}_\mathrm{s}} \boldsymbol{V}_\mathrm{sq}(t)\,dt. \tag{9}$$

The integrals on the right side of the above equation can be approximated via the forward Euler method (Seborg et al. (2016)) which, for a generic continuous-time signal $s(t) \in \mathbb{R}$, amounts to:

$$\int_{k\cdot\mathcal{T}_\mathrm{s}}^{(k+1)\cdot\mathcal{T}_\mathrm{s}} s(t)\,dt \approx \tilde{s}(k;\mathcal{T}_\mathrm{s}) \cdot \mathcal{T}_\mathrm{s}. \tag{10}$$

However, we point out that (10) is not suited for the integral $\int_{k\cdot\mathcal{T}_\mathrm{s}}^{(k+1)\cdot\mathcal{T}_\mathrm{s}} \boldsymbol{V}_\mathrm{sq}(t)\,dt$ in (9). That is because the voltage PWM signals are sampled at a sampling time $\mathcal{T}_\mathrm{s} = \mathcal{T}_\mathrm{P}^{(1)}$, leading the forward Euler method to miss the portions of the signals when the voltages are zero and, consequently, to a suboptimal approximation (see Fig. 3). Consequently, we propose an ad hoc discretization method for PWM signals that are sampled at a sampling time that is equal to their PWM period. Consider the squared voltages $V_i^{(r)}(t)^2, i \in \{1,2\}, r \in \{1,2\}$. We propose the following approximation (see (6) and (7)):

$$\int_{k\cdot\mathcal{T}_\mathrm{s}}^{(k+1)\cdot\mathcal{T}_\mathrm{s}} V_i^{(r)}(t)^2\,dt \approx \tilde{V}_\mathrm{g}(k;\mathcal{T}_\mathrm{s})^2 \cdot \tilde{\mathcal{T}}_{\mathrm{ON}_i}^{(r)}(k;\mathcal{T}_\mathrm{s}) \approx \tilde{V}_\mathrm{g}(k;\mathcal{T}_\mathrm{s})^2 \cdot \tilde{u}_i^{(r)}(k;\mathcal{T}_\mathrm{s}) \cdot \mathcal{T}_\mathrm{s}. \tag{11}$$

As highlighted in Fig. 3, the approximation in (11) is better suited for computing the integral of the squared voltages in (9) compared to (10). To discretize the system in (5), we apply the forward Euler method to the integrals that concern $\boldsymbol{q}^{(\mathrm{f})}(t)$, $\boldsymbol{T}(t)$, and $T_\mathrm{a}(t)$. Instead the integral related to $\boldsymbol{V}_\mathrm{sq}(t)$ is approximated using (11). The resulting sampled-data state-space model is:

$$\begin{cases} \tilde{\boldsymbol{q}}^{(\mathrm{f})}(k+1;\mathcal{T}_\mathrm{s}) = \tilde{A}_{ff} \cdot \tilde{\boldsymbol{q}}^{(\mathrm{f})}(k;\mathcal{T}_\mathrm{s}) + \tilde{B}_f \cdot \tilde{\boldsymbol{u}}(k;\mathcal{T}_\mathrm{s}) \cdot \tilde{V}_\mathrm{g}(k;\mathcal{T}_\mathrm{s})^2 \\ \tilde{\boldsymbol{T}}(k+1;\mathcal{T}_\mathrm{s}) = \tilde{A}_{TT} \cdot \tilde{\boldsymbol{T}}(k;\mathcal{T}_\mathrm{s}) + \tilde{A}_{Tf} \cdot \tilde{\boldsymbol{q}}^{(\mathrm{f})}(k;\mathcal{T}_\mathrm{s}) + \tilde{\boldsymbol{b}}_T \cdot \tilde{T}_\mathrm{a}(k;\mathcal{T}_\mathrm{s}) \\ \tilde{\boldsymbol{y}}(k;\mathcal{T}_\mathrm{s}) = \tilde{\boldsymbol{T}}(k;\mathcal{T}_\mathrm{s}) \end{cases} \tag{12}$$

where the matrices and vectors amount to:
$\tilde{A}_{ff} = A_{ff} \cdot \mathcal{T}_\mathrm{s} + I_4, \tilde{A}_{ff} \in \mathbb{R}^{4\times4}$, $\tilde{B}_f = B_f \cdot \mathcal{T}_\mathrm{s}, \tilde{B}_f \in \mathbb{R}^{4\times4}$,
$\tilde{A}_{TT} = A_{TT} \cdot \mathcal{T}_\mathrm{s} + I_6, \tilde{A}_{TT} \in \mathbb{R}^{6\times6}$, $\tilde{A}_{Tf} = A_{Tf} \cdot \mathcal{T}_\mathrm{s}, \tilde{A}_{Tf} \in \mathbb{R}^{6\times4}$,
$\tilde{\boldsymbol{b}}_T = \boldsymbol{b}_T \cdot \mathcal{T}_\mathrm{s}, \tilde{\boldsymbol{b}}_T \in \mathbb{R}^6$,
and $I_m, m \in \mathbb{N}$, is the $m \times m$ identity matrix. In what follows, we will refer to the model in (12) as discretized Electro-eQuivalent Thermal Model (dEQTM). One of the advantages of the proposed approximation method in (11) compared to forward Euler in (10) is that the dependency on the control actions, i.e. the duty cycles $\tilde{\boldsymbol{u}}(k;\mathcal{T}_\mathrm{s})$, is made explicit in the dEQTM, easing controller design.

4. IDENTIFICATION OF THE PARAMETERS

The dEQTM in (12) depends on several unknown parameters: the thermal resistances $R_i^{(l)}, R_{\mathrm{T}_i}^{(l')}, R_{\mathrm{T}_{12}}, R_{\mathrm{T}_{21}}, i \in \{1,2\}, l \in \{1,2,3\}, l' \in \{1,2\}$, the thermal capacitance C_z, the time constants $\tau_i, i \in \{1,2\}$, and the resistance R_heat (see Section 3). In practice, C_z need not be estimated; assuming that we are dealing with dry air at constant pressure, we have (Halliday et al. (2013)):

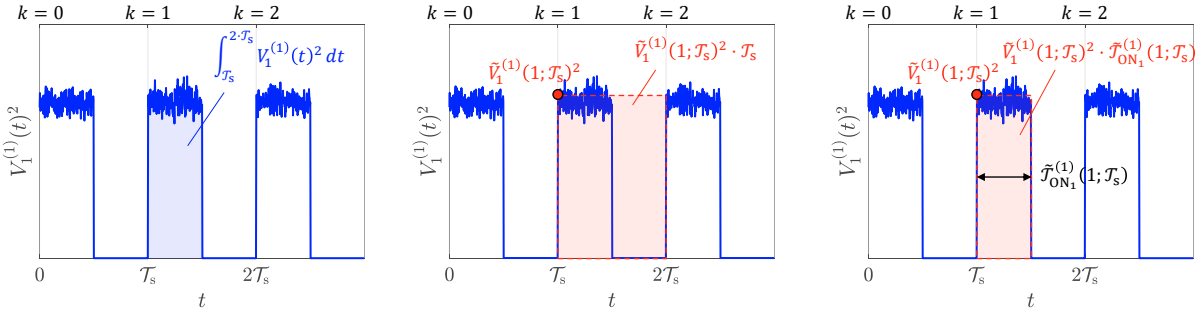

(a) - Real integral. **(b) - Forward Euler method.** **(c) - Proposed method.**

Fig. 3. Comparison between the forward Euler method in (10) and the proposed method in (11) when approximating the integral $\int_{k\cdot\mathcal{T}_s}^{(k+1)\cdot\mathcal{T}_s} V_1^{(1)}(t)^2\,dt$. The fluctuations in $V_1^{(1)}(t)$ are due to the fluctuations in the grid voltage $V_g(t)$.

$$C_z = c_{air}\cdot\rho_{air}\cdot\frac{\mathcal{V}_{oven}}{6} = 461\,\frac{J}{°C},$$

where $c_{air} = 1000\,\frac{J}{Kg\cdot°C}$ is the specific heat of air, $\rho_{air} = 1.225\,\frac{Kg}{m^3}$ is the air density, and $\mathcal{V}_{oven} = 2.26\,m^3$ is the volume of the oven cavity. We group all the unknown parameters inside a vector $\boldsymbol{\theta}\in\mathbb{R}^{n_\theta}_{>0}$, which are $n_\theta = 15$ in total. $\boldsymbol{\theta}$ is estimated using data coming from five experiments carried out on the shrink tunnel under study:

- (E1) Open-loop step response test with $\tilde{u}_i^{(r)}(k;\mathcal{T}_s) = 0.5, \forall k\in\mathbb{N}\cup\{0\}$, and $i\in\{1,2\}, r\in\{1,2\}$;
- (E2) Open-loop step response test with $\tilde{u}_1^{(r)}(k;\mathcal{T}_s) = 0.5, \tilde{u}_2^{(r)}(k;\mathcal{T}_s)=0, \forall k\in\mathbb{N}\cup\{0\}$, and $r\in\{1,2\}$;
- (E3) Open-loop step response test with $\tilde{u}_1^{(r)}(k;\mathcal{T}_s) = 0, \tilde{u}_2^{(r)}(k;\mathcal{T}_s)=0.5, \forall k\in\mathbb{N}\cup\{0\}$, and $r\in\{1,2\}$;
- (E4) Closed-loop test where only the temperatures $T_1^{(1)}$ and $T_2^{(2)}$ are controlled in closed-loop by PID controllers. Specifically, the regulators are tasked to track a piecewise constant reference signal that alternates between 160°C and 150°C .
- (E5) Closed-loop step response test with reference signal equal to 160°C and different PID tunings compared to (E4).

These experiments were designed with the following goals in mind: (i) each trial must take less than a work day, (ii) a wide temperature range should be covered, and (iii) some experiments should capture typical closed-loop operation, making them suited for the identification of a control-oriented model.

Let $N_E = 5$ be the number of experiments and $N_E^{(e)}\in\mathbb{N}, e\in\{1,\dots,N_E\}$, be the number of samples acquired in the e-th experiment. Then, we estimate $\boldsymbol{\theta}$ according to the output-error approach (Verhaegen and Verdult (2007)), i.e. by minimizing the following cost function over $\mathbb{R}^{n_\theta}_{>0}$:

$$J(\boldsymbol{\theta}) = \frac{1}{N_E}\sum_{e=1}^{N_E}\left[\frac{1}{N_E^{(e)}}\sum_{k=0}^{N_E^{(e)}-1}\left\|\tilde{\boldsymbol{y}}^{(e)}(k;\mathcal{T}_s) - \hat{\tilde{\boldsymbol{y}}}^{(e)}(k;\mathcal{T}_s,\boldsymbol{\theta})\right\|_2^2\right], \quad (13)$$

where $\tilde{\boldsymbol{y}}^{(e)}(k;\mathcal{T}_s)$ are the measured outputs of the e-th experiment at index $k\in\{0,\dots,N_E^{(e)}-1\}$, while $\hat{\tilde{\boldsymbol{y}}}^{(e)}(k;\mathcal{T}_s,\boldsymbol{\theta})$ are the outputs estimated by the dEQTM in (12), simulated using the inputs $\tilde{\boldsymbol{u}}^{(e)}(k;\mathcal{T}_s)$, $\tilde{T}_a^{(e)}(k;\mathcal{T}_s)$, and $\tilde{V}_g^{(e)}(k;\mathcal{T}_s)$, associated with the e-th experiment. At the beginning of all the experiments, the temperatures are at equilibrium and are equal to the (constant) ambient temperature $\bar{T}_a$, while the heat resistors are off. Consequently, we can remove $\bar{T}_a$ from each output $\tilde{\boldsymbol{y}}^{(e)}(k;\mathcal{T}_s)$ and neglect $\tilde{T}_a^{(e)}(k;\mathcal{T}_s)$ when simulating $\hat{\tilde{\boldsymbol{y}}}^{(e)}(k;\mathcal{T}_s,\boldsymbol{\theta})$. Specifically, for any $\boldsymbol{\theta}\in\mathbb{R}^{n_\theta}_{>0}$, the initial states of the model in (12) are set to zero and need not be estimated, i.e. $\hat{\tilde{\boldsymbol{q}}}^{(f),(e)}(0;\mathcal{T}_s,\boldsymbol{\theta}) = \boldsymbol{0}_4$ and $\hat{\tilde{\boldsymbol{T}}}^{(e)}(0;\mathcal{T}_s,\boldsymbol{\theta}) = \boldsymbol{0}_6$. Then, we compute $\hat{\tilde{\boldsymbol{q}}}^{(f),(e)}(k;\mathcal{T}_s,\boldsymbol{\theta})$ and $\hat{\tilde{\boldsymbol{T}}}^{(e)}(k;\mathcal{T}_s,\boldsymbol{\theta})$ at any $k\in\{1,\dots,N_E^{(e)}-1\}$ and for any $e\in\{1,\dots,N_E\}$ by iterating the state equations in (12) using only $\tilde{\boldsymbol{u}}^{(e)}(k;\mathcal{T}_s)$ and $\tilde{V}_g^{(e)}(k;\mathcal{T}_s)$. Finally, we set $\hat{\tilde{\boldsymbol{y}}}^{(e)}(k;\mathcal{T}_s,\boldsymbol{\theta}) = \hat{\tilde{\boldsymbol{T}}}^{(e)}(k;\mathcal{T}_s,\boldsymbol{\theta}), \forall k\in\{0,\dots,N_E^{(e)}-1\}, \forall e\in\{1,\dots,N_E\}$, and calculate the cost defined in (13).

Comparatively, we also consider an additional model obtained by approximating the relationship between each temperature (output) and each duty cycle (input) using a FOLPD transfer function (He et al. (2014)). In particular, consider the j-th output $y_j(t), j\in\{1,\dots,6\}$, and the input $u_i^{(r)}(t), i\in\{1,2\}, r\in\{1,2\}$. Then:

$$G_{ji}^{(r)}(s) = \frac{Y_j(s)}{U_i^{(r)}(s)} = \frac{\mu_{ji}^{(r)}}{1+s\cdot\tau_{ji}^{(r)}}\cdot\exp\left\{-s\cdot L_{ji}^{(r)}\right\}, \quad (14)$$

where $\mu_{ji}^{(r)}\in\mathbb{R}_{>0}$ (in °C) is the gain, $\tau_{ji}^{(r)}\in\mathbb{R}_{>0}$ is the time constant (in s), and $L_{ji}^{(r)}\in\mathbb{R}_{\geq 0}$ is the time delay (in s). We group the parameters of the 24 FOLPD transfer functions inside a vector $\boldsymbol{\theta}\in\mathbb{R}^{n_\theta}_{\geq 0}$ ($n_\theta = 72$ in total) and we estimate them via the output-error approach for continuous-time systems. Specifically, we apply the maximum likelihood method discussed in Garnier (2015), i.e., analogously to (13), we minimize the difference between the measured and simulated outputs in the Least Squares sense, averaged over the N_E experiments.

5. EXPERIMENTAL RESULTS

Now, we assess the performances of the derived models on a validation dataset resulting from a closed-loop experiment that was not used during the identification described in Section 4. Let $\hat{\boldsymbol{\theta}}\in\mathbb{R}^{n_\theta}_{\geq 0}$ be the estimated parameters of either the dEQTM in (12) or the FOLPD model in (14). Moreover, let $\tilde{\epsilon}_j^{(v)}\left(k;\mathcal{T}_s,\hat{\boldsymbol{\theta}}\right), j\in\{1,\dots,6\}$, be the error

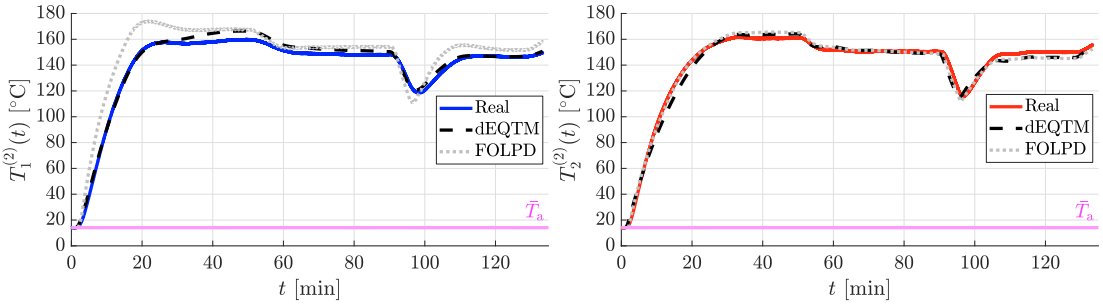

		$T_1^{(3)}$ $(j=1)$	$T_1^{(2)}$ $(j=2)$	$T_1^{(1)}$ $(j=3)$	$T_2^{(1)}$ $(j=4)$	$T_2^{(2)}$ $(j=5)$	$T_2^{(3)}$ $(j=6)$	**Average**
$\text{Fit}_j^{(\text{v})}$ [%]	dEQTM	96.88%	**97.56%**	**97.10%**	95.75%	97.38%	**97.93%**	**97.10%**
	FOLPD	**97.37%**	91.91%	95.79%	**96.97%**	**97.92%**	95.31%	95.88%
$\text{MaxErr}_j^{(\text{v})}$ [°C]	dEQTM	8.56	**7.18**	**10.43**	**10.26**	9.58	**6.29**	**8.72**
	FOLPD	**7.45**	27.71	22.40	11.32	**6.66**	18.38	15.66

Fig. 4. Performances of the dEQTM in (12) and the FOLPD model in (14) on the validation dataset w.r.t. the indicators in (15) and (16). The best results are highlighted with a bold font. We also show the simulated outputs corresponding to $T_1^{(2)}$ and $T_2^{(2)}$, for which either the dEQTM or the FOLPD model notably outperformed the other.

made by the identified models on the j-th output $\tilde{y}_j^{(\text{v})}$ of the validation dataset at index k, i.e.:

$$\tilde{\epsilon}_j^{(\text{v})}\left(k;\mathcal{T}_\text{s},\hat{\boldsymbol{\theta}}\right)=\tilde{y}_j^{(\text{v})}\left(k;\mathcal{T}_\text{s}\right)-\hat{\tilde{y}}_j^{(\text{v})}\left(k;\mathcal{T}_\text{s},\hat{\boldsymbol{\theta}}\right).$$

Finally, let $N^{(\text{v})}\in\mathbb{N}$ be the number of samples present in the validation dataset. We evaluate the performances using the following measures of goodness: (i) the fits, i.e.

$$\text{Fit}_j^{(\text{v})}=1-\frac{\sqrt{\frac{1}{N^{(\text{v})}}\cdot\sum_{k=0}^{N^{(\text{v})}-1}\left|\tilde{\epsilon}_j^{(\text{v})}\left(k;\mathcal{T}_\text{s},\hat{\boldsymbol{\theta}}\right)\right|^2}}{\max_k\tilde{y}_j^{(\text{v})}(k;\mathcal{T}_\text{s})-\min_k\tilde{y}_j^{(\text{v})}(k;\mathcal{T}_\text{s})},\qquad(15)$$

and (ii) the maximum absolute errors, i.e.

$$\text{MaxErr}_j^{(\text{v})}=\max_k\left|\tilde{\epsilon}_j^{(\text{v})}\left(k;\mathcal{T}_\text{s},\hat{\boldsymbol{\theta}}\right)\right|\quad[^\circ\text{C}].\qquad(16)$$

The performances achieved by the dEQTM in (12) and the FOLPD model in (14) on the validation dataset are reported in Fig. 4. We can clearly see that (on average) the proposed model outperforms its competitor w.r.t. both (15) and (16). In particular, the FOLPD model exhibits maximum absolute errors that exceed 20°C while the dEQTM shows a $\text{MaxErr}_j^{(\text{v})}$ that is, at most, roughly 11°C. Instead, the fits are overall comparable. We conclude that the proposed model in (12) clearly outperforms the one in (14), especially if we also take into account that it uses 4.8 times fewer parameters ($n_\theta=15$ against $n_\theta=72$).

6. CONCLUSIONS

This paper presented a lumped-parameter sampled-data state-space model for the industrial oven of a shrink tunnel. The model has been derived following the thermal-electrical analogy and via a novel and ad hoc discretization strategy. Its parameters have been estimated following the output-error approach, using data coming from an extensive experimental campaign. The proposed model exhibited better performances on experimental data compared to the FOLPD model with notably fewer parameters.

REFERENCES

Garnier, H. (2015). Direct continuous-time approaches to system identification. Overview and benefits for practical applications. *Eur. J. control*, 24, 50–62.

Halliday, D., Resnick, R., and Walker, J. (2013). *Fundamentals of physics*. John Wiley & Sons.

He, W., Xu, G., and Shen, R. (2014). Control of temperature uniformity in the temperature chamber with centrifugal acceleration. *J. Process Control*, 24(12), 1–6.

Ramirez-Laboreo, E., Sagues, C., and Llorente, S. (2016). Dynamic heat and mass transfer model of an electric oven for energy analysis. *Appl. Therm. Eng.*, 93, 683–691.

Rastegarpour, S., Gros, S., and Ferrarini, L. (2020). Mpc approaches for modulating air-to-water heat pumps in radiant-floor buildings. *Control Eng. Pract.*, 95, 104209.

Ryckaert, V.G., Claes, J.E., and Van Impe, J.F. (1999). Model-based temperature control in ovens. *J. Food Eng.*, 39(1), 47–58.

Seborg, D.E., Edgar, T.F., Mellichamp, D.A., and Doyle III, F.J. (2016). *Process dynamics and control*. John Wiley & Sons.

Serale, G., Fiorentini, M., Capozzoli, A., Bernardini, D., and Bemporad, A. (2018). Model predictive control (mpc) for enhancing building and hvac system energy efficiency: Problem formulation, applications and opportunities. *Energies*, 11(3), 631.

Sidebotham, G. (2015). *Heat Transfer Modeling*. Springer.

Terzi, E., Bonetti, T., Saccani, D., Farina, M., Fagiano, L., and Scattolini, R. (2020). Learning-based predictive control of the cooling system of a large business centre. *Control Eng. Pract.*, 97, 104348.

Tudon-Martinez, J.C., Cantu-Perez, A., Cardenas-Romero, A., and Lozoya-Santos, J.d.J. (2019). Mathematical model-based design of an industrial box furnace. *Appl. Therm. Eng.*, 161, 114153.

Vasičkaninová, A., Bakošová, M., Mészáros, A., and Klemeš, J.J. (2011). Neural network predictive control of a heat exchanger. *Appl. Therm. Eng.*, 31(13), 2094–2100.

Verhaegen, M. and Verdult, V. (2007). *Filtering and system identification: a least squares approach*. Cambridge University Press.